Temperature-dependent spectral emittance of bauxite and silica particle beds

Chuyang Chen, Chiyu Yang, Kevin Pan, Devesh Ranjan,

Peter G. Loutzenhiser, and Zhuomin M. Zhang

George W. Woodruff School of Mechanical Engineering, Georgia Institute of Technology, Atlanta, United States

Bauxite and silica particles are candidate materials for solar thermal energy storage at high temperatures. The temperature-dependent emittance of packed beds with bauxite and silica particles was measured using a newly upgraded emissometer at wavelengths 2 μ m $\leq \lambda \leq$ 16 μ m and temperatures up to ~730 K. The room-temperature emittance was obtained from the measured directional-hemispherical reflectance. A fused silica disc was used to test the emissometer by comparing the measured spectral emittance with the calculated emittance from a fitted Lorentz oscillator model. For the polycrystalline silica particles and the fused silica disc, the measured emittance increases with temperature in the mid-infrared region. The underlying mechanism is interpreted as the temperature-dependent damping coefficient in the Lorentz oscillator model. Two types of bauxite particles with different compositions and sizes were investigated. For $\lambda > 10~\mu$ m, the measured emittance at elevated temperatures is higher than that at room temperature. In the region 2 μ m $< \lambda < 6~\mu$ m, the temperature dependence varies for different types of particles. The total emittance of bauxite particle beds was calculated by spectral integration using Planck's distribution at the prescribed temperature. The calculated total emittance is between 0.89 and 0.96, but it does not change monotonically with temperature.

KEYWORDS: Emittance, high temperature, particle bed, radiative properties

Contact: Zhuomin M. Zhang: <u>zhuomin.zhang@me.gatech.edu</u> George W. Woodruff School of Mechanical Engineering, Georgia Institute of Technology, Atlanta, United States

1

Introduction

Bauxite and silica solid particles are promising candidates for solar thermal energy storage (TES) media in concentrating solar power (CSP) applications due to their high temperature stability and large heat capacitance without phase change [1-3]. Falling particle receiver using particles with high solar absorptance is one of the viable options to deliver low cost, environmentally friendly, and long-term production of electricity [1, 4]. In a typical particle receiver, concentrated solar radiation from a heliostats field is focused on a particle curtain and directly absorbed by the particles [5, 6]. The temperature of the particles reaches 700–1000 °C, depending on the specific setup and the type of particles being used [4, 7]. The absorbed solar energy is stored in the form of sensible heat [2, 8]. This provides flexibility for electricity production even during nighttime, which is not favored in traditional photovoltaics. Nevertheless, the particle curtain absorbs radiative energy via complex mechanisms that include direct absorption, scattering between particles, and re-radiation by the walls of the particle receiver cavity [9-11]. The intrinsic spectral radiative properties of the particles play an instrumental role in accurately estimating the receiver efficiency.

Continuous progress has been made in measuring the spectral and total radiative properties of solid particles and packed beds [12-16]. Bauxite particles that mainly contain Al_2O_3 and some SiO_2 (with the addition of various Fe, Mn, and Cr oxides to enhance solar absorption) have been extensively studied for CSP applications [4, 5, 17-24]. The solar absorptance of Al_2O_3 -based or SiO_2 -based sand particles is typically less than 0.70, which is too low for use as a direct solar absorber [18]. Siegal et al. [5] measured the spectral reflectance of several types of Carbobead particles for wavelengths between 0.3 μ m < λ < 2.0 μ m. These particles are sintered bauxite proppants manufactured by Carbo Ceramic Co. with high strength and roundness [25]. The as-

received particles possess a solar absorptance (calculated from the reflectance) exceeds 0.90 [4, 5], similar to that of a previous studied type of bauxite particles [17]. Chen et al. [21] used a windowed method to measure the spectral reflectance of Carbobead particles for 0.4 μ m < λ < 15 μ m and observed high solar absorptance (0.94–0.96) for beds of different particle sizes. A model based on effective medium theory was used to explain the integral role of Fe₂O₃ in the absorption of solar radiation in the visible-to-near-infrared (NIR) region [21]. The scattering albedo, extinction coefficient, and the absorptive index of several bauxite materials in the form of hot-pressed plate were studied for 1.5 μ m < λ < 2.5 μ m [23]. The scattering phase function of several Carbobead particles has been characterized as nearly isotropic [24]. These results are of great importance to accurately model other thermophysical properties such as thermal conductivity in particle beds [26], and the overall heat transfer modeling of a particle receiver [27].

Relatively few experimental works have been performed to examine and quantify the radiative properties of particles or particle beds at elevated temperatures. The total emittance has often been obtained by spectral integration based on the spectral reflectance measured at room temperature [4, 5, 18, 21]. In most of the modeling approaches, a constant emittance was assigned to the particles. Such assumption may potentially result in unrealistic predictions that deviate from experiments when modeling heat transfer processes of the particle receiver at elevated temperatures [27-29]. Typically, either a direct or an indirect method is used for measuring the spectral emittance of films and bulk materials [30-35]. However, there are daunting challenges for directly measuring the high-temperature emittance of particles or particle beds due to their nonhomogeneous structure, which could result in a large temperature gradient within the measured layer thickness [36-39]. Some researchers have investigated the directional emittance of nonisothermal and isothermal particle beds by considering the relations between the directional

emittance and the temperature gradient, porosity, and particle face temperature [40-42]. Wald and Salisbury [43] measured the directional emittance of the powdered quartz considering the exitance angle, particle size, and packing condition. A non-contact measurement technique based on blackbody distribution and directional reflectance was demonstrated by Meneses et al. [44] and used to study thin films and rough surfaces. When the particle diameter is of several millimeters, direct measurement of the total emittance and absorption function of individual particles (Al₂O₃ and SiC) has also been performed [45]. There is an urgent need for direct measurements of the spectral emittance of solid particles at elevated temperatures and in the mid-infrared region.

In the present work, an in-house spectral emissometer facility is upgraded to include a sample chamber with a horizontally mount heater to hold the particle samples in a flat crucible made of copper. The Christiansen wavelength and known spectral feature were used to determine the surface temperature and to self-correct for misalignment error. The measurement technique was validated with a fused silica disc. The spectral emittance of particle beds with polycrystalline silica particles and several bauxite (Carbobead) particles was directly measured at temperatures up to ~730 K, and the results were compared to the room-temperature emittance calculated from the measured directional-hemispherical reflectance. The total emittance of the bauxite particle beds was also calculated at the corresponding temperatures.

Metrology and validation

Emissometer setup

The measurement apparatus consists of a sample chamber, a blackbody cavity, several windows and mirrors, and an ABB FTLA2000 Fourier-transform infrared spectrometer (FTIR), as shown in Figure 1a. A side view of the sample chamber is shown in Figure 1b. This setup is a modified design of the previous setup for measuring the emittance of flat plate samples [33]. The

packed bed is positioned horizontally for direct measurement of the emission signal from the heated particles. A quartz plate covers a horizontally placed electric heater, which is embedded in the refractory insulation with a cylindrical opening pocket. A flat Cu crucible sits in the pocket on the quartz plate. A side hole was drilled into the base of the crucible and a thermocouple was inserted through the insulation all the way to the center of the crucible without toughing the particles. The crucible holds either the particle beds or a bulk disc with a diameter of approximately 25 mm and a depth of 2-5 mm. The particles in the bed was lightly compressed by a flat surface to remove any unevenness. The sample stage is enclosed in a stainless-steel chamber with a transparent ZnSe window for emission output. For optical equivalency, a ZnSe window was also placed in front of the blackbody box (not shown in Figure 1a). The chamber shields the sample from air current disturbances and provides a stable environment. The normal thermal emission signal (with a half cone angle of 3°) is reflected by the 45° angle plane mirror atop the sample to form a horizontal beam, which is then sent through the ZnSe window to the elliptical mirror. The second focus of the elliptical mirror is at the iris. The beam expands after the iris to the parabolic mirror and is reflected as a collimated beam into the FTIR through a build-in ZnSe window on the side (emission) port.

The optical components are enclosed by an acrylic box and purged with nitrogen gas to diminish the effect of spectral absorption lines by H₂O(v) and CO₂. A plane mirror is mounted on a motorized linear translation stage, which moves the mirror in and out of the optical path to switch the emission source between the blackbody and the sample when needed. The optical path from the sample to the FTIR and that from the blackbody to the FTIR were designed to be equal with identical number of transmissions and reflections. The various mirrors in the optical path were coated with Au film to achieve high infrared reflectance and long-term stability. The iris placed

between the ellipsoid mirror and the parabolic mirror eliminates out-of-focus irradiation. The spectral range of the FTIR measurements is 1 μ m $< \lambda <$ 19 μ m with a deuterated triglycine sulfate (DTGS) detector and ZnSe windows.

The optical system was aligned with a laser pointer placed horizontally. It sends a red light reversely through the parabolic mirror, iris, ellipsoidal mirror, and then to the sample surface (or the blackbody opening). The plane mirrors mounted on the linear stage and above the heated sample merely alter the irradiation direction, while maintaining the same total path length and optical efficiency from the sample (or the opening of the blackbody) to the ellipsoid mirror. When the laser sends a collimated beam to the parabolic mirror, a small spot is expected to show at the location of the sample surface (or the blackbody opening) and is visible by blocking the light path with a white paper. Despite carefully design and alignment efforts, imperfect positioning of the mirrors, FTIR, sample holder, and the blackbody may result in some optical inequivalence. In addition, there exists a relatively large temperature gradient within the sample, especially with the particle bed. The emission signal comes from not only the top layer of the particles but also the adjacent particle layers due to light scattering. This also causes optical inequivalence as the optical design shown in Figure 1a presumes that the emission is from the sample surface. The aperture size of the iris may also influence the measurements. A large aperture improves the signal-to-noise ratio but at the same time gives rise to misalignment that deteriorates the optical equivalence. A trade-off must be made and the final aperture diameter is approximately 3 mm. Overall, a 10–15% inequivalence should be expected. A post-processing method that uses a correction factor is developed and will be explained in the data analysis section.

A Mikron M360 blackbody with a 25 mm aperture diameter was used as the reference source with a temperature accuracy of \pm 1 K and a stability of \pm 0.5 K . A PID controller

regulates the blackbody temperature. The system produces thermal emission with nearly 99.99% of the blackbody limit. An example of the measured blackbody spectra, $S_{BB}(\lambda, T)$ at T = 473 K, 673 K, and 873 K (200 °C, 400 °C, and 600 °C), respectively, is shown in Figure 2. The spectral resolution of the FTIR was set to 4 cm⁻¹. The results were averaged for 512 scans with additional piecewise data smoothing process to remove noises. The signal strength is very low for $\lambda < 2 \mu m$ and $\lambda > 16$ µm, especially at relatively low temperatures. Therefore, the measured spectrum was truncated to 2 μ m $\leq \lambda \leq$ 16 μ m with reasonable spectral response. The signal unit is arbitrary and it does not affect the final result because the emittance is obtained from the ratio of the sample signal to the blackbody signal at the same temperature. Due to the wavelength dependence of the detector response, optics, and signal processing method in the FTIR measurements, the peak wavelength in the measured spectra does not correspond to the prediction by Wein's displacement law. A broadband H₂O(v) absorption in the region 5 μ m < λ < 8 μ m is observed and becomes more significant at elevated temperatures. There appears to be a narrowband absorption line about 4.3 μm due to the presence of CO₂, causing significant signal drop. When reporting the measured emittance, the artifact associated with the spectral absorption line near 4.3 µm was removed through post-processing.

The crucible temperature, $T_{\rm cru}$, measured by the inserted thermocouple is always higher than the surface temperature of the particle bed due to the low thermal conductivity of the particles and contact resistances [26]. Nevertheless, $T_{\rm cru}$ provides an indication of the sample temperature and was used as a set point to control the heater with a PID temperature controller using LabView. During the measurement, the crucible was set to $T_{\rm cru}=200~{\rm ^{\circ}C}$, 400 ${\rm ^{\circ}C}$, and 600 ${\rm ^{\circ}C}$. Because the exact emission location and temperature profile of the sample are unknown, an effective sample

temperature T needs to be determined so that the spectral emittance of the sample is calculated from the ratio of the sample signal to the blackbody signal at the wavelength and same temperature. The details are to be discussed in the session on data analysis. The stainless-steel sample chamber may operate under evacuated condition with a pressure below 10^{-4} Pa to minimize convective heat loss. However, it was found that free convection helps improve temperature uniformity in the particle beds. Therefore, all measurements were performed at ambient pressure condition to obtain the sample emission signal, $S(\lambda, T)$.

The FTIR was also used for measuring the specular reflectance (at 10° incidence) of the fused silica disc at room temperature when using the internal Globar (SiC) source with proper accessories [46]. For the particle beds, an integrating sphere was used to measure the room-temperature directional-hemispherical reflectance with the FTIR [21, 47]. The emittance at room temperature was calculated from the reflectance in the opaque region. The uncertainty in emittance at room temperature was estimated based on the reflectance measurements to be 0.02 for silica disc and 0.03 for particle beds. The lab temperature is typically 22–25 °C. It is expected that a small temperature change will not affect the radiative properties of the sample. Hence, the room temperature is indicated as 300 K throughout this paper.

Data analysis

The normal emittance of the sample is determined from the measured quantities using the following equation:

$$\varepsilon(\lambda, T) = \frac{1}{F_{\rm C}} \frac{S(\lambda, T) - S_0(\lambda)}{S_{\rm BB}(\lambda, T) - S_{\rm BB, 0}(\lambda)} \tag{1}$$

Here, $S(\lambda,T)$ and $S_{\mathrm{BB}}(\lambda,T)$ are the sample and blackbody emission signals at the same temperature, respectively, $S_0(\lambda)$ and $S_{\mathrm{BB},0}(\lambda)$ are the background signals when the sample and blackbody are at the ambient temperature, and F_{C} is a correction factor to account for the inequivalence between the optical paths during the measurements. Ideally, F=1; however, due to imperfect alignment and varying properties of the mirrors and windows, an inequivalence exists between the optical paths that must be considered. In practical situations with the room-temperature DTGS detector, S_0 and $S_{\mathrm{BB},0}$ are negligibly small compared with the emission signals at T>450 K and hence are ignored hereafter.

As mentioned previously, due to low thermal conductivity of the particle beds (0.25–0.50 W/m·K) [26] and the contact thermal resistance between the particles and the Cu crucible, a relatively large temperature gradient is present in the particle bed. The surface temperature cannot be predicted by modeling due to the unknown thermal contact resistance, boundary condition at the top surface of the particle bed, and heat transfer rate through the particle bed. Efforts were made by inserting a thermocouple near the top surface of the particles. However, the measurement is not sufficiently reliable due to the large thermal contact resistance and difficulties in determine the exact thermocouple location. Due to the unknown emittance of the particle bed surface, pyrometer measurements also yielded a relatively large uncertainty. Therefore, the effective sample temperature *T* is determined using the following procedure.

Because the temperature of the sample is treated as an unknown, this presents some challenges in setting the blackbody to be at the same temperature. In the measurements, the blackbody emission spectra are taken at several discrete temperatures. Interpolation is needed to determine the blackbody spectrum at a given temperature T using the measured emission spectra at T_1 and T_2 , with $T_1 < T < T_2$. However, a simple linear interpolation results in a large uncertainty

and even changed the spectral characteristics. Assume $S_{\rm BB}(\lambda,T)$ is proportional to the spectral intensity $I_{\rm b,\lambda}(\lambda,T)$ given by Planck's distribution. A proper interpolation formula reads:

$$\frac{S_{\text{BB}}(\lambda, T) - S_{\text{BB}}(\lambda, T_1)}{S_{\text{BB}}(\lambda, T_2) - S_{\text{BB}}(\lambda, T_1)} = \frac{I_{\text{b},\lambda}(\lambda, T) - I_{\text{b},\lambda}(\lambda, T_1)}{I_{\text{b},\lambda}(\lambda, T_2) - I_{\text{b},\lambda}(\lambda, T_1)}$$
(2)

This relationship holds as long as the detector spectral response is linear and consistent. Equation (2) was validated by measuring the blackbody emission spectra at three different temperatures. If the right-hand side of Eq. (2) were replaced by $(T-T_2)/(T_1-T_2)$, the result would not be acceptable.

For oxide materials, the emittance (or absorptance) is very close to 1 at the Christiansen wavelength, $\lambda_{\rm Ch}$, which is typically in the mid-infrared where the refractive index is approximately equal to 1 [48]. Based on Eq. (1), if the background signals are neglected and $\varepsilon(\lambda_{\rm Ch},T)=1$, then,

$$S(\lambda_{\rm Ch}, T) = F_{\rm C}S_{\rm BB}(\lambda_{\rm Ch}, T) \tag{3}$$

In Eq. (3), $S_{\rm BB}(\lambda_{\rm Ch},T)$ is evaluated using Eq. (2) and taken as a known quantity at prescribed temperature. If $F_{\rm C}$ is known, Eq. (3) enables the determination of the sample temperature T. In the setup used, $F_{\rm C}$ varies from 1.10 to 1.15 and is somewhat sample dependent. Additional information about the spectral shape or multiple peaks was used to evaluate $F_{\rm C}$. An iterative procedure is used to determine both $F_{\rm C}$ and T. A guess value of $F_{\rm C}$ was used as the trial value. Then T is determined from Eq. (3) by solving the combined equations. The spectral shape or peaks were analyzed to further tuning $F_{\rm C}$ until satisfactory agreement is achieved. For the fused silica disc and silica particle bed, the Christiansen wavelength is at $\lambda_{\rm Ch} = 7.30~\mu m$. $F_{\rm C} = 1.15~{\rm was}$

obtained by comparison of the measured spectra with the literature for fused silica [30]. For the bauxite particles, based on both room-temperature and high-temperature measurements, the emittance is close to 1 in a broad spectral region due to multiple phonon oscillators in the composite material [21]. $F_{\rm C}$ =1.11 was obtained from the broadband emittance peak observed for one type of particles, specifically, Carbobead CP 30/60 at room temperature. Once determined, $F_{\rm C}$ is kept constant throughout the measurements for other bauxite particle beds. Due to the temperature nonuniformity and inequivalence, the overall uncertainty of the direct emittance measurements was estimated to be 0.03 for fused silica disc and 0.05 for all particle beds.

Validation with a fused silica disc

The fused silica disc with 99.995% purity was purchased from McMaster Carr (https://www.mcmaster.com/1357T21) and used to test the method of temperature determination and alignment correction of the emissometer. The disc is 25 mm in diameter and 3 mm in thickness. The room-temperature reflectance and transmittance of the disc were measured using the FTIR with its internal emission source. The normal-normal transmittance and specular reflectance at 10° were measured. Since the disc is smooth, the measured properties are essentially directional-hemispherical. The measured room-temperature reflectance R and transmittance T are shown in Figure 3, and compared with the model predictions based on the tabulated optical constants [49]. Fused silica is transparent in the short wavelength region up to $\lambda \approx 3.5 \, \mu \text{m}$ and becomes opaque at $\lambda \approx 4.75 \, \mu \text{m}$, as shown in Figure 3b. As the wavelength increases, the reflectance decreases to zero at the Christiansen wavelength of $\lambda_{\text{Ch}} = 7.30 \, \mu \text{m}$ and increases to reach a peak at $\lambda \approx 8.9 \, \mu \text{m}$ due to lattice vibration and there is a weak phonon feature at $\sim 13 \, \mu \text{m}$. Overall, the model prediction is

in good agreement with the measurement results. The small deviations near $2.5 \mu m$ and $3.7 \mu m$ are attributed to sample-to-sample variation (e.g., slightly varying impurities introduced during different fabrication processes).

For high-temperature emittance measurements, with $\lambda_{\rm Ch} = 7.30~\mu{\rm m}$ and $F_{\rm C} = 1.15$, the surface temperature of the fused silica disc is obtained as T = 446 K, 610 K, and 769 K at the set point of the crucible $T_{\rm cru}$ = 473 K, 673 K, and 873 K, respectively. The large temperature difference is principally caused by the contact resistance, in addition to the temperature gradient in the fused silica. The measured emittance spectra are shown in Figure 4a at $\lambda > 5 \, \mu m$. Because the fused silica is semitransparent at $\lambda < 5 \,\mu m$, the emission signal in short wavelength region is dominated by thermal emission from the Cu crucible surface. The emittance for 300 K is calculated from the room-temperature reflectance based on Kirchhoff's law using $\varepsilon = 1 - R$, where (1 - R) is the absorptance since only the opaque region is of interest [48]. The temperature-dependent phonon structure yields an increase of emittance as the temperature is increased. This effect was observed by Rozenbaum et al. [30] and explained by the associated increase in the damping coefficient of the phonon with a resonance frequency of 1100 cm⁻¹ (9.1 µm). To quantify such effect, the measured emittance spectra were fitted to a Lorentz oscillator model with three oscillators (phonon modes) in the present study. The complex dielectric function $\tilde{\epsilon}$ as a function of frequency ω in [cm⁻¹] is described as follows:

$$\tilde{\iota} + \sum_{j=1}^{3} \frac{S_j \omega_j^2}{\omega_j^2 - i\gamma_j \omega - \omega^2} \tag{4}$$

where ε_{∞} is a high-frequency constant, and S_j , ω_j , and γ_j are the strength, resonance frequency, and damping coefficient of the j^{th} oscillator, respectively. The Lorenz model is an implementation

of the equation of motion for lattice vibration considering bound electrons [48]. It is difficult to model the dielectric function of SiO₂ in the mid-infrared due to multiple resonances [50], though a simple Lorentz model with only two oscillators was used to capture the resonance feature at 1100 cm⁻¹ and 460 cm⁻¹, respectively [51]. In the present study, since the spectral region of interest is 5 $\mu m < \lambda < 18$ μm , three oscillators with $\omega_1 = 779.1$ cm⁻¹, $\omega_2 = 1100$ cm⁻¹, and $\omega_3 = 1188$ cm⁻¹ were used based on the least-squares fitting at room temperature. The value of $\varepsilon_{\infty} = 2.568$ was also obtained from fitting the room-temperature result. This value is slightly higher than those based on n^2 of fused silica, which is near 2.1 at $\lambda < 1$ µm [49]. The resonance frequencies and ε_{∞} are assumed to be independent of temperature. Only the strength and damping coefficients of the three oscillators are tuned to fit the emittance at elevated temperatures. The best-fitted parameters are listed in Table 1, and the predicted emittance spectra are displayed in Figure 4b at the corresponding temperatures. Although the fitting has uncertainties associated with the experiments and the model itself, the Lorentz model captures the main features and the temperature dependence of emittance when comparing Figure 4b and 4a. As expected, the main change in the oscillator parameters comes from the damping coefficient γ_2 , which has a nearly twofold increase from T=300 K to 769 K. This is the main reason accounting for the enhancement of emittance in the region $8 \, \mu \text{m} < \lambda < 10 \, \mu \text{m}$ as temperature increases. The trend and magnitude of measured emittance of fused silica are in qualitative agreement with those reported in Ref. [30] at high temperatures.

Results and discussion

Particle sample description

Two types of particles were investigated and their images from a microscope are shown in Figure 5. All particles are nearly spherical with some surface irregularities and size variation. The

polycrystalline silica particles (Wedron 410 from Wedron Co.) have an average diameter d=222 μ m and a purity of 99.65% (https://www.lancasterfoundrysupply.com/pdf/wedron_silica.pdf). The silica particles appear to be clear and transparent with slight but discernible impurities that could affect the absorption in the visible and semitransparent region, as discussed previously [52]. The bauxite or alumina-silica particles are Carbobead manufactured by Carbo Ceramic Co. They are made of Al₂O₃, TiO₂, SiO₂ and Fe₂O₃ with somewhat different mass fractions and porosity. The average diameters of CP 30/60 and CP 50/140 are 453 μ m and 194 μ m, respectively, and those of HSP 30/60 and HSP 16/30 are 495 μ m and 956 μ m, respectively. The Carbobead particles appear dark to the naked eye under regular lighting conditions, unlike what the images from the microscope show. Detailed description and the measurement of the radiative properties of the bauxite particles are available in Ref. [21]. The thickness of the packed bed is approximately 3 mm for all particles contained in the Cu crucible. Test measurements were also performed for certain particles with varying thicknesses, and it was found that 3 mm thickness is sufficient to achieve complete opacity.

Emittance of the silica bed

In a recent work [52], the room-temperature radiative properties for several types of silica particles were measured and modeled. Polycrystalline silica materials are expected to have similar transparent windows like fused silica [49, 53]. The emittance of the Wedron 410 particle bed at various temperatures is shown in Figure 6 for $\lambda > 5$ µm, where the packed bed is opaque due to the high absorption coefficient and scattering effect of silica particles. Again, the emittance at 300 K was calculated from 1 - R. Since the HgCdTe detector was used for the room-temperature reflectance measurements, the cutoff wavelength is ~15 µm. For the high-temperature

measurements with the DTGS detector, the spectra extend to 16 μ m (beyond which the noise is very high). Note that the ordinate begins at ε = 0.4. For the same crucible temperatures, the "surface" temperature of the particle bed is 435 K, 583 K, and 713 K, much lower than that with the fused silica disc especially at the highest temperature setting due to the low effective thermal conductivity of the particle bed. There are some fluctuations in the spectra at elevated temperatures, especially for T = 435 K due to the low signal-to-noise ratio.

Crystalline silica (often referred to as quartz) is anisotropic with different phonon structures for ordinary and extraordinary rays [53-55]. It is reasonable to expect that the dielectric function of polycrystalline particles is described by the effective medium theory based on the ordinary and extraordinary dielectric functions [21]. Using the model dielectric function, Chen et al. [52] predicted the reflectance of a polycrystalline silica plate. From the room-temperature result, the Christiansen wavelength was determined to be $\lambda_{\rm Ch}=7.35~\mu{\rm m}$. The particle bed exhibits a lower reflectance or higher emittance than the quartz plate in the phonon absorption region for 8 $\mu{\rm m}<\lambda<10~\mu{\rm m}$. As shown in Figure 6, the measured emittance of the particle bed in the 8–10 $\mu{\rm m}$ region increases as the temperature goes up and the emittance peak at 8.7 $\mu{\rm m}$ diminishes towards high temperatures. The observed trend agrees well with the previous studies of α -quartz for ordinary rays [54, 55]. It has been shown that the phonon mode at 1154 cm⁻¹ (~8.7 $\mu{\rm m}$) is not observable above 846 K, when quartz changes from α -phase to β -phase [54, 55].

At λ > 9.5 µm, the measured emittance at elevated temperatures almost overlap with each other, suggesting weak temperature effects on the emittance in this spectral region. The room-temperature emittance is about 0.03 lower for 9.5 µm < λ < 12.5 µm and 0.05 lower at λ > 13 µm when compared with the average emittance at the three elevated temperatures. The indirect measurement at room temperature used the windowed method is subject to some uncertainties due

to the contact conditions between the particles and the window. The difference between room-temperature and high-temperature emittance at longer wavelengths is potentially due to measurement errors from both methods. From a theoretical point of view, there exists a second emittance peak at 12.3 μ m with ε = 0.98 according to the effective medium theory. Interestingly, this feature is well captured by the high-temperature emittance. The silica bed results provide further evidence that the high-temperature emissometer setup and data processing method are capable of accurately measuring the infrared emittance of particle beds.

Emittance of bauxite ceramic particle bed

The measured emittance spectra of packed beds are shown in Figures 7 and 8 for selected CP and HSP particles, respectively, with different sizes. The 300 K results are calculated from the directional-hemispherical reflectance reported previously [21]. Due to the low signal-to-noise ratio in the spectral when $T_{\rm cru}=473~{\rm K}$, high-temperature emittance spectra are plotted only for $T_{\rm cru}=673~{\rm K}$ and 873 K for all four packed beds. Similar to the silica particles, a large temperature difference between $T_{\rm cru}$ and T is observed. On the average, $\Delta T = T_{\rm cru} - T = 86.5~{\rm K}$ when $T_{\rm cru}=673~{\rm K}$ and $\Delta T=155~{\rm K}$ when $T_{\rm cru}=873~{\rm K}$. Overall the emittance of Carbobeads particles is quite high, noting that the minimum of ordinate is 0.70. The measurements were validated through repeating measurements over a period of time, though all particle samples are as received. No notable changes were observed through repeating measurements of the same batch of particles after several heating cycles.

For the bed packed with CP 30/60 particles, as shown in Figures 7a, there is a shift of the Christiansen wavelength towards longer wavelength from 8.0 µm at room temperature to 8.5 µm

at elevated temperatures. Due to multiple phonon features associated with the constituent materials, there is a broadband emittance peak from 8–10 $\mu m,$ which enables the determination of $\it T$ and $\it F_{\rm C}$. There is another peak near 9.5 μ m. Even at T = 587 K, the spectrum at $\lambda < 3$ μ m is very noisy and exceeds 1 towards shorter wavelengths. The short wavelength cutoff wavelength for the hightemperature emittance spectrum is set to $\lambda = 2 \mu m$. A valley in the region $2 \mu m < \lambda < 6 \mu m$ is present with a minimum about 4 µm at all temperatures for both CP 30/60 and CP 50/140. The large dip in the emittance for CP 50/140 has been discussed in the previous work [21], presumably due to the longer penetration depth and enhanced scattering by small particles. The measured emittance around $\lambda = 4 \mu m$ for CP 50/140 increases by about 0.1 from room temperature to high temperatures. This was presumably a result of the temperature nonuniformity within the particle bed and the relatively large penetration depth with small particles. Additional emission from lower particle layers at higher temperatures may produce a relatively large emission signal. The exact reason requires further investigation. Similar to those with the silica particles, at wavelengths longer than 9.5 µm, the emittance at elevated temperatures is always higher than that at room temperature. The difference is less than 0.03 for 9.5 μ m < λ < 13 μ m and about 0.05 beyond 13 um. It may be caused by the temperature-dependent phonon structures or by measurement uncertainties. It is unlikely that free carriers have any impact on the high-temperature emittance since Carbobead particles are made of refractory materials with very large band gaps.

For HSP particle beds, as shown in Figure 8, the long-wavelength trend is similar to that of CP particle beds, with a broadband peak that is slightly shifted towards longer wavelengths at elevated temperatures. The peak emittance occurs about $\lambda = 10 \,\mu m$ at high temperatures. At $\lambda > 9.5 \,\mu m$, the emittance is similar at the two elevated temperatures and higher than that at room temperature by similar magnitude as for CP and silica particle beds. What is surprising is that there

appears to be a reduction of emittance for 3 $\mu m < \lambda < 6$ μm for both HSP 30/60 and HSP 16/30 at high temperatures, resulting in a shift of the emittance minimum from near 2.5 μm to near 4 μm . The feature of this valley becomes similar to those with CP 30/60 particles. The mechanisms for causing such a strong temperature dependence in HSP particle beds is not yet clear and worth further investigation. Possible reasons are the change of chemical composition, porosity, as well as sintering and thermal stress effect. There are limited work reporting the effect of thermal stress and degradation of radiative properties due to thermal cycling. Siegal et al. [5] observed that thermal cycling Carbobead HSP particles over 500 hours at 1000 °C causes reduction in the absorptance for $\lambda < 2.5$ μm , especially towards 2.5 μm . In the present study, the particle temperatures are much lower and the heating duration is much shorter, although the emittance was measured directly at elevated temperatures.

Total emittance of bauxite particle beds

The total normal emittance at a given temperature is calculated by weighting over the Planck distribution such that [48]

$$\varepsilon(T) = \frac{I(T)}{I_{b}(T)} = \frac{\pi}{\sigma T^{4}} \int_{0}^{\infty} \varepsilon(\lambda, T) I_{b, \lambda}(\lambda, T) d\lambda$$
 (5)

where I is total intensity of the sample, $I_{\rm b} = \sigma T^4/\pi$ is the blackbody intensity in a vacuum, and σ is the Stefan-Boltzmann constant. For the Carbobead particle bed, the hemispherical emittance is expected to be close the normal emittance due to the topographic arrangement and surface roughness. The measured spectral range covers approximately 2.5 μ m < λ < 16 μ m with the high-temperature emissometer and 0.4 μ m < λ < 15 μ m at 300 K. In order to facilitate reasonable calculations of the total emittance, the room-temperature spectral emittance for λ < 1.8 μ m is used

to extend the high-temperature emittance toward shorter wavelengths and a constant value is assumed for $\lambda > 16$ µm (same as the emittance at $\lambda = 16$ µm). The transition region is linearly interpolated between $\lambda = 1.8$ µm (from T = 300 K) and $\lambda = 3.0$ µm (from high-temperature results) to further reduce the effect of low signal-to-noise ratio towards $\lambda = 2.0$ µm in the high-temperature data.

The calculated total emittance at each temperature is tabulated in Table 2 for packed beds with the four types of Carbobead particles. The total emittance is not evaluated for the silica particle bed due to semitransparency. For the same crucible temperature, the particle bed may have different effective sample temperatures as indicated in parentheses. The sample temperature T is used when integrating the total emittance using Eq. (5). As $T_{\rm cru}$ increases from 300 K to 673 K and 873 K, $\varepsilon(T)$ is shown to increase and then decrease slightly. The increase is due to the higher spectral emittance at high temperatures compared to that of the room temperature, especially at longer wavelength. The decrease of the total emittance when T_{cru} increases from 673 K to 873 K is due to the shift of the Planck's blackbody emission peak towards short wavelength, coupled to a reduced spectral emittance towards 4 µm. The change, however, is not as significant. Except for HSP 16/30 whose emittance increases from 0.890 at 300 K to 0.958 at 586 K, and then reduces to 0.944 at 719 K. The emittance of other packed beds increases by 0.03 (for $T_{\rm cru}$ from 300 K to 673 K) and decreases by less than 0.02 (for $T_{\rm cru}$ from 673 K to 873 K). Overall, the total emittance varies from 0.89 to 0.96. Using the room-temperature spectral emittance to calculate the total emittance at elevated temperatures would result in a maximum difference of 0.04 (for CP50/140) in the predicted total emittance. The overall difference is small due to the already high emittance of the bauxite particles.

The maximum achievable sample temperature (T = 726 K) for the bauxite particle bed is limited by experiment setup in this work due to the limitations of the heater and the ambient pressure condition. Nevertheless, this work offers the first quantitative direct measurements of the spectral emittance of bauxite particle beds. The quantitative results may help refine the heat transfer modeling of the particle-to-particle and particle-to-wall radiation transfer processes.

Conclusions

The spectral normal emittance of bauxite and silica particle beds of different sizes were measured for 2 μ m < λ < 16 μ m at effective bed temperatures up to ~730 K. A noncontact temperature determination technique was used to calculate effective sample temperature and the associated blackbody reference signal. Validations of the setup was performed using a homogenous fused silica disc. The increase of the emittance in the infrared region (8 μ m < λ < 10 μ m) at higher temperatures was attributed to increases in the damping coefficients. Similar temperature dependent features were also observed for silica particle beds. For bauxite particle beds, in the wavelength region 3 μ m < λ < 7 μ m, the emittance increases at high temperatures for CP particle beds, whereas the emittance decreases for HSP particle beds. Both CP and HSP particle beds have an increase emittance towards longer wavelengths (λ > 9.5 μ m). The total emittance for CP and HSP particle beds at different temperatures was calculated with an average over 0.90. This work provides quantitative information on the high-temperature radiative properties of particle beds and facilitates the analysis of the particle-to-particle and particle-to-wall radiation transfer processes for concentrating solar power systems with falling particle receivers.

Acknowledgements

This work was supported by the U.S. Department of Energy's Office of Energy Efficiency and Renewable Energy (EERE) under Solar Energy Technologies Office Award Number EE0008372. C.Y. was supported by the National Science Foundation (CBET-2029892). The views expressed herein do not necessarily represent the views of the U.S. Department of Energy, National Science Foundation, or the United States Government. The author would also like to thank Shomik Verma and Malavika V. Bagepalli for their help in the experiments.

Disclosure statement. The authors report there are no competing interests to declare.

Data availability. The data that support the findings of this study are available upon request from the corresponding author with reasonable request.

Nomenclature

d = average particle diameter, mm

 $F_{\rm C}$ = correction factor

 $I = \text{total intensity, W/m}^2 \cdot \text{sr}$

 $I_{b,\lambda}$ = blackbody spectral intensity, W/m²· μ m·sr

R = directional-hemispherical reflectance

S = measured emission signal, arbitrary units

 S_0 = measured ambient noise signal, arbitrary units

 S_i = oscillator strength

T = effective temperature of the particle bed, K

 $T_{\rm cru}$ = temperature of the crucible, K

Greek

 γ_j = damping coefficient, cm⁻¹

 ε = spectral emittance

 $\tilde{\ell}$ = complex dielectric function

 ε_{∞} = high-frequency constant

 λ = wavelength, μ m

 $\lambda_{\rm Ch}$ = Christiansen wavelength, μm

 ω = frequency, cm⁻¹

 ω_j = resonance frequency, cm⁻¹

Subscripts

BB = blackbody source

b = blackbody

References

- [1] A. Gil, *et al.*, "State of the art on high temperature thermal energy storage for power generation. Part 1—Concepts, materials and modellization," *Renew. Sustain. Energy Rev.*, vol. 14, no. 1, pp. 31–55, 2010. https://doi.org/10.1016/j.rser.2009.07.035
- [2] C. K. Ho, "A review of high-temperature particle receivers for concentrating solar power," *Appl. Therm. Eng.*, vol. 109, part B, pp. 958–969, 2016. https://doi.org/10.1016/j.applthermaleng.2016.04.103
- [3] W. Lipiński, *et al.*, "Progress in heat transfer research for high-temperature solar thermal applications," *Appl. Therm. Eng.*, vol. 184, pp. 116137, 2021. https://doi.org/10.1016/j.applthermaleng.2020.116137
- [4] N. P. Siegel, M. D. Gross, C. K. Ho, T. Phan, and J. Yuan, "Physical properties of solid particle thermal energy storage media for concentrating solar power applications," *Energy Procedia*, vol. 49, pp. 1015–1023, 2014. https://doi.org/10.1016/j.egypro.2014.03.109
- [5] N. P. Siegel, M. D. Gross, and R. Coury, "The development of direct absorption and storage media for falling particle solar central receivers," *J. Sol. Energy Eng.*, vol. 137, no. 4, pp. 041003, 2015. https://doi.org/10.1115/1.4030069
- [6] C. K. Ho, *et al.*, "On-sun performance evaluation of alternative high-temperature falling particle receiver designs," *J. Sol. Energy Eng.*, vol. 141, no. 1, pp. 011009, 2019. https://doi.org/10.1115/1.4041100
- [7] Z. Ma, G. Glatzmaier, and M. Mehos, "Fluidized bed technology for concentrating solar power with thermal energy storage," *J. Sol. Energy Eng.*, vol. 136, no. 3, pp. 031014, 2014. https://doi.org/10.1115/1.4027262
- [8] T. Baumann and S. Zunft, "Properties of granular materials as heat transfer and storage medium in CSP application," *Sol. Energy Mater. Sol. Cells*, vol. 143, pp. 38–47, 2015. https://doi.org/10.1016/j.solmat.2015.06.037
- [9] G. Evans, W. Houf, R. Greif, and C. Crowe, "Gas-particle flow within a high temperature solar cavity receiver including radiation heat transfer," *J. Sol. Energy Eng.*, vol. 109, no. 2, pp. 134–142, 1987. https://doi.org/10.1115/1.3268190
- [10] A. Kumar, J.-S. Kim, and W. Lipiński, "Radiation absorption in a particle curtain exposed to direct high-flux solar irradiation," *J. Sol. Energy Eng.*, vol. 140, no. 6, pp. 061007, 2018. https://doi.org/10.1115/1.4040290
- [11] N. P. Siegel, C. K. Ho, S. S. Khalsa, and G. J. Kolb, "Development and evaluation of a prototype solid particle receiver: On-sun testing and model validation," *J. Sol. Energy Eng.*, vol. 132, no. 2, pp. 021008, 2010. https://doi.org/10.1115/1.4001146
- [12] C. L. Tien, "Thermal radiation in packed and fluidized beds," *J. Heat Transfer*, vol. 110, no. 11, pp. 1230–1242, 1988. https://doi.org/10.1115/1.3250623
- [13] B. M. Agarwal and M. P. Mengüç, "Forward and inverse analysis of single and multiple scattering of collimated radiation in an axisymmetric system," *Int. J. Heat Mass Transfer*, Vol. 34, no. 3, pp. 633–647, 1991. https://doi.org/10.1016/0017-9310(91)90112-R

- [14] K. Kamiuto, M. Iwamoto, M. Sato, and T. Nishimura, "Radiation-extinction coefficients of packed-sphere systems," *J. Quant. Spectrosc. Radiat. Transfer*, Vol. 45, no. 2, pp. 93–96, 1991. https://doi.org/10.1016/0022-4073(91)90103-W
- [15] P. Coray, W. Lipiński, and A. Steinfeld, "Spectroscopic goniometry system for determining thermal radiative properties of participating media," *Exp. Heat Transfer*, vol. 24, no. 4, pp. 300–312, 2011. https://doi.org/10.1080/08916152.2011.556311
- [16] K. Ganesan, J. Randrianalisoa, and W. Lipiński, "Effect of morphology on spectral radiative properties of three-dimensionally ordered macroporous ceria packed bed," *J. Heat Transfer*, vol. 135, no. 12, pp. 122701, 2013. https://doi.org/10.1115/1.4024942
- [17] J. Griffin, K. Stahl, and R. Pettit, "Optical properties of solid particle receiver materials: I. Angular scattering and extinction characteristics of Norton Masterbeads®," Sol. Energy Mater., vol. 14, nos. 3-5, pp. 395–416, 1986. https://doi.org/10.1016/0165-1633(86)90062-6
- [18] J. Roop, S. Jeter, S. I. Abdel-Khalik, and C. K. Ho, "Optical properties of select particulates after high-temperature exposure," *Proc. ASME 8th Inernational Conference on Energy Sustainability*, Paper No. ES2014-6504, 2014, https://doi.org/10.1115/ES2014-6504
- [19] J. Marti, M. Roesle, and A. Steinfeld, "Experimental determination of the radiative properties of particle suspensions for high-temperature solar receiver applications," *Heat Transfer Eng.*, vol. 35, no. 3, pp. 272–280, 2014. https://doi.org/10.1080/01457632.2013.825173
- [20] D. Mischler and A. Steinfeld, "Nonisothermal nongray absorbing-emitting-scattering suspension of Fe₃O₄ particles under concentrated solar irradiation," *J. Heat Transfer*, vol. 117, no. 2, pp. 346–354, 1995. https://doi.org/10.1115/1.2822528
- [21] C. Chen, C. Yang, D. Ranjan, P. G. Loutzenhiser, and Z. M. Zhang, "Spectral radiative properties of ceramic particles for concentrated solar thermal energy storage applications," *Int. J. Thermophys.*, vol. 41, pp. 152, 2020. https://doi.org/10.1007/s10765-020-02733-5
- [22] B. Gobereit, L. Amsbeck, C. Happich, and M. Schmücker, "Assessment and improvement of optical properties of particles for solid particle receiver," *Solar Energy*, vol. 199, no. 3, pp. 844–851, 2020. https://doi.org/10.1016/j.solener.2020.02.076
- [23] J. Chen, *et al.*, "Optical and radiative characterisation of alumina–silica based ceramic materials for high-temperature solar thermal applications," *J. Quant. Spectrosc. Radiat. Transfer*, vol. 272, pp. 107754, 2021. https://doi.org/10.1016/j.jqsrt.2021.107754
- [24] S. Y. Jeong, C. Chen, D. Ranjan, P. G. Loutzenhiser, and Z. M. Zhang, "Measurements of scattering and absorption properties of submillimeter bauxite and silica particles," *J. Quant. Spectrosc. Radiat. Transfer*, vol. 276, pp. 107923, 2021. https://doi.org/10.1016/j.jqsrt.2021.107923
- [25] M. V. Bagepall, et al., "Measurement of flow properties coupled to experimental and numerical analyses of dense, granular flows for solar thermal energy storage," Solar Energy, vol. 207, pp. 77–90, 2020. https://doi.org/10.1016/j.solener.2020.06.062

- [26] K. M. Chung, *et al.*, "Measurement and analysis of thermal conductivity of ceramic particle beds for solar thermal energy storage," *Sol. Energy Mater. Sol. Cells*, vol. 230, pp. 111271, 2021. https://doi.org/10.1016/j.solmat.2021.111271
- [27] E. F. Johnson, I. Tari, and D. Baker, "Modeling heat exchangers with an open source DEM-based code for granular flows," *Solar Energy*, vol. 228, pp. 374–386, 2021. https://doi.org/10.1016/j.solener.2021.09.067
- [28] J. Martinek and Z. Ma, "Granular flow and heat-transfer study in a near-blackbody enclosed particle receiver," *J. Sol. Energy Eng.*, vol. 137, no. 5, pp. 051008, 2015. https://doi.org/10.1115/1.4030970
- [29] W. Wang, Y. Shuai, B. G. Lougou, and B. Jiang, "Thermal performance analysis of free-falling solar particle receiver and heat transfer modelling of multiple particles," *Appl. Therm. Eng.*, vol. 187, pp. 116567, 2021. https://doi.org/10.1016/j.applthermaleng.2021.116567
- [30] O. Rozenbaum, D. D. S. Meneses, Y. Auger, S. Chermanne, and P. Echegut, "A spectroscopic method to measure the spectral emissivity of semi-transparent materials up to high temperature," *Rev. Sci. Instrum.*, vol. 70, no. 10, pp. 4020–4025, 1999. https://doi.org/10.1063/1.1150028
- [31] L. del Campo, R. B. Pérez-Sáez, X. Esquisabel, I. Fernández, and M. J. Tello, "New experimental device for infrared spectral directional emissivity measurements in a controlled environment," *Rev. Sci. Instrum.*, vol. 77, no. 11, pp. 113111, 2006. https://doi.org/10.1063/1.2393157
- [32] C. P. Cagran, L. M. Hanssen, M. Noorma, A. V. Gura, and S. N. Mekhontsev, "Temperature-resolved infrared spectral emissivity of SiC and Pt-10Rh for temperatures up to 900°C," *Int. J. Thermophys.*, vol. 28, no. 2, pp. 581–597, 2007. https://doi.org/10.1007/s10765-007-0183-1
- [33] L. P. Wang, S. Basu, and Z. M. Zhang, "Direct measurement of thermal emission from a Fabry–Perot cavity resonator," *J. Heat Transfer*, vol. 134, no. 7, pp. 072701, 2012. https://doi.org/10.1115/1.4006088
- [34] I. Setién-Fernández, *et al.*, "First spectral emissivity study of a solar selective coating in the 150–600°C temperature range," *Sol. Energy Mater. Sol. Cells*, vol. 117, pp. 390–395, 2013. https://doi.org/10.1016/j.solmat.2013.07.002
- [35] S. Shan, *et al.*, "Spectral emittance measurements of micro/nanostructures in energy conversion: A review," *Front. Energy*, vol. 14, no. 3, pp. 482–509, 2020. https://doi.org/10.1007/s11708-020-0693-0
- [36] G. Flamant, "Theoretical and experimental study of radiant heat transfer in a solar fluidized-bed receiver," *AIChE J.*, vol. 28, no. 4, pp. 529–535, 1982. https://doi.org/10.1002/aic.690280402
- [37] K. A. Stahl, J. W. Griffin, and R. B. Pettit, "Optical properties of solid particle receiver materials: II. Diffuse reflectance of Norton Masterbeads® at elevated temperatures," *Sol. Energy Mater.*, vol. 14, no. 3-5, pp. 417–425, 1986. https://doi.org/10.1016/0165-1633(86)90063-8

- [38] J. Yamada and Y. Kurosaki, "Estimation of a radiative property of scattering and absorbing media," *Int. J. Thermophys.*, vol. 18, no. 2, pp. 547–556, 1997. https://doi.org/10.1007/BF02575183
- [39] A. Sielaff, *et al.*, "Temperature measurement using infrared thermometry within semi-transparent media," *Exp. Heat Transfer*, vol. 32, no. 6, pp. 545–565, 2019. https://doi.org/10.1080/08916152.2018.1549622
- [40] P. Jones, D. McLeod, and D. Dorai-Raj, "Correlation of measured and computed radiation intensity exiting a packed bed," *J. Heat Transfer*, vol. 118, no. 1, pp. 94–102, 1996. https://doi.org/10.1115/1.2824073
- [41] D. Baillis and J.-F. Sacadura, "Directional spectral emittance of a packed bed: Influence of the temperature gradient in the medium," *J. Heat Transfer*, vol. 124, no. 5, pp. 904–911, 2002. https://doi.org/10.1115/1.1466459
- [42] R. R. Lopes, L. M. Moura, D. Baillis, and J.-F. Sacadura, "Directional spectral emittance of a packed bed: Correlation between theoretical prediction and experimental data," *J. Heat Transfer*, vol. 123, no. 2, pp. 240–248, 2001. https://doi.org/10.1115/1.1338134
- [43] A. E. Wald and J. W. Salisbury, "Thermal infrared directional emissivity of powdered quartz," *J. Geophys. Res.*, vol. 100, no. B12, pp. 24665–24675, 1995. https://doi.org/10.1029/95JB02400
- [44] D. D. S. Meneses, P. Melin, L. del Campo, O. Rozenbaum, and L. Cosson, "Probing high temperature thermal emissive properties of energy materials and coatings with emission spectroscopy augmented by in situ reflection," *Infrared Phys. Technol.*, vol. 108, pp. 103329, 2020. https://doi.org/10.1016/j.infrared.2020.103329
- [45] W. Zhao, Z. Sun, and Z. T. Alwahabi, "Emissivity and absorption function measurements of Al₂O₃ and SiC particles at elevated temperature for the utilization in concentrated solar receivers," *Solar Energy*, vol. 207, pp. 183–191, 2020. https://doi.org/10.1016/j.solener.2020.06.079
- [46] S. Basu, B. J. Lee, and Z. M. Zhang, "Infrared radiative properties of heavily doped silicon at room temperature," *J. Heat Transfer*, vol. 132, no. 2, pp. 023301, 2010. https://doi.org/10.1115/1.4000171
- [47] Q. Cheng, P. Yang, Z. M. Zhang, "Radiative properties of ceramic Al₂O₃, AlN, and Si₃N₄—I. Experiments," *Int. J. Thermophys.*, vol. 37, pp. 62, 2016. https://doi.org/10.1007/s10765-016-2067-8
- [48] Z. M. Zhang, *Nano/Microscale Heat Transfer*, Springer Nature Switzerland AG, 2nd ed., 2020.
- [49] H. R. Philipp, "Silicon Dioxide (SiO₂) (Glass)," in *Handbook of Optical Constants of Solids*, edited by E. D. Palik, Academic Press Imprint, 1998, pp. 749–763.
- [50] R. Kitamura, L. Pilon, and M. Jonasz, "Optical constants of silica glass from extreme ultraviolet to far infrared at near room temperature," *Appl. Opt.*, vol. 46, no. 33, pp. 8118–8133, 2007. https://doi.org/10.1364/AO.46.008118

- [51] D.-Z. A. Chen, R. Hamam, M. Soljačić, J. D. Joannopoulos, and G. Chen, "Extraordinary optical transmission through subwavelength holes in a polaritonic silicon dioxide film," *Appl. Phys. Lett.*, vol. 90, no. 18, pp. 181921, 2007. https://doi.org/10.1063/1.2736267
- [52] C. Chen, C. Yang, D. Ranjan, P. G. Loutzenhiser, and Z. M. Zhang, "Spectral radiative properties of polydispersed SiO₂ particle beds," *J. Thermophys. Heat Transfer* (published online https://doi.org/10.2514/1.T6524).
- [53] H. R. Philipp, "Silicon dioxide (SO₂), type α (crystalline)," in *Handbook of Optical Constants of Solids*, edited by E. D. Palik, Academic Press Imprint, 1998, pp. 719–747.
- [54] S. Zeidler, Th. Posch, and H. Mutschke, "Optical constants of refractory oxides at high temperatures: Mid-infrared properties of corundum, spinel, and α-quartz, potential carriers of the 13 μm feature," *Astronomy & Astrophys.*, vol. 553, pp. A81, 2013. https://doi.org/10.1051/0004-6361/201220459
- [55] F. Gervais and B. Piriou, "Temperature dependence of transverse and longitudinal optic modes in the α and β phases of quartz," *Phys. Rev. B*, vol. 11, no. 10, pp. 3944–3950, 1975. https://doi.org/10.1103/PhysRevB.11.3944

Table 1. Parameters in the Lorentz oscillator model obtained by fitting the emittance of fused silica disc. The sample temperature is in parentheses. Note that $\varepsilon_{\infty}=2.568$.

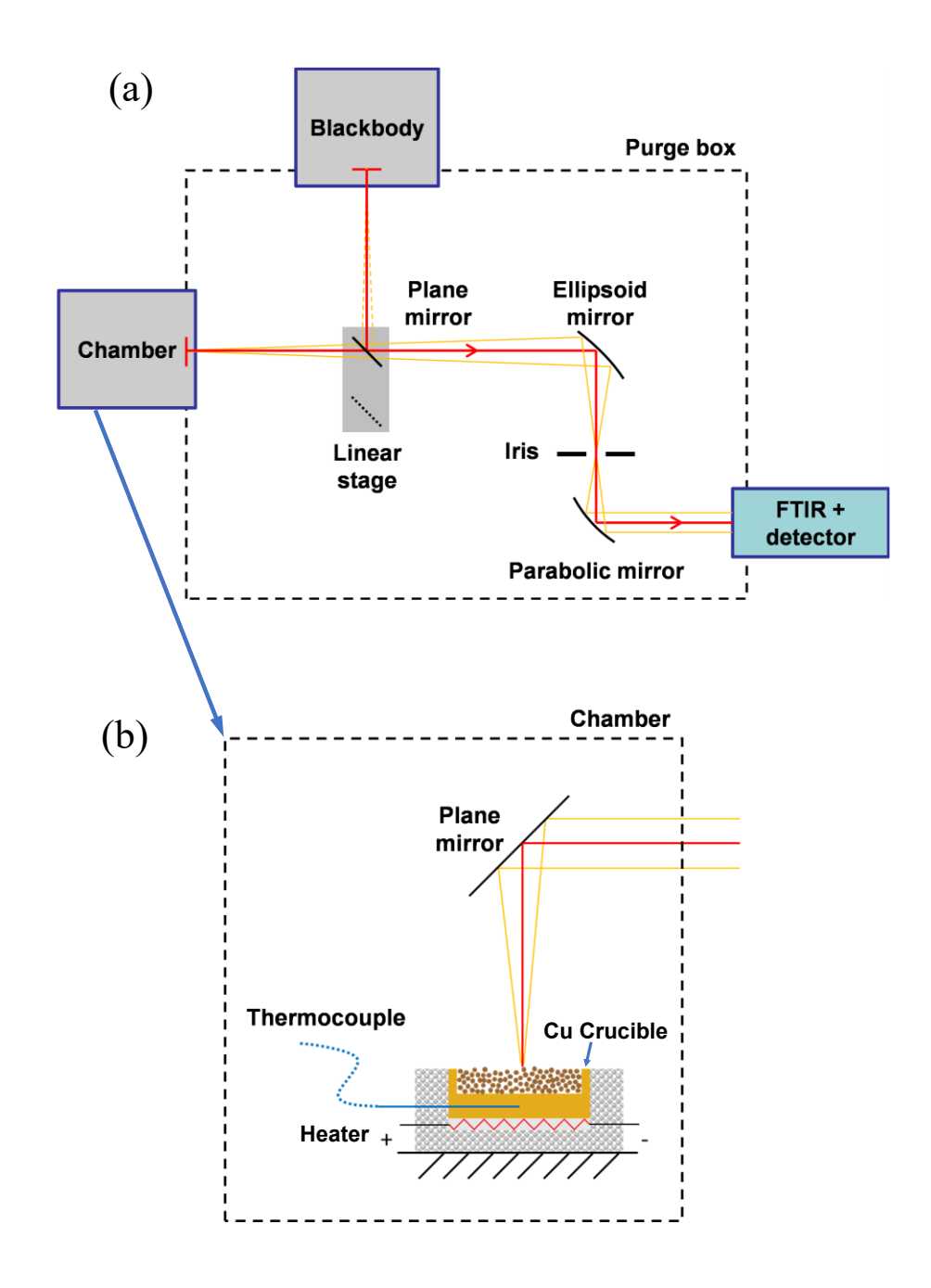
	Ambient	$T_{\rm cru} = 473 \text{ K}$	$T_{\rm cru} = 673 \text{ K}$	$T_{\rm cru} = 873 \text{ K}$
	(300 K)	(T = 446 K)	(T = 610 K)	(T = 769 K)
ω_1	799.1	799.1	799.1	799.1
S_1	0.034	0.031	0.026	0.020
γ_1	34.49	32.48	35.90	32.48
ω_2	1100	1100	1100	1100
S_2	0.585	0.553	0.513	0.483
γ_2	22.95	30.07	36.02	41.06
ω_3	1188	1188	1188	1188
S_3	0.099	0.105	0.111	0.103
γ_3	87.82	89.59	94.68	92.30

Table 2. Total emittance of the bauxite particle beds. The sample temperature is in parentheses.

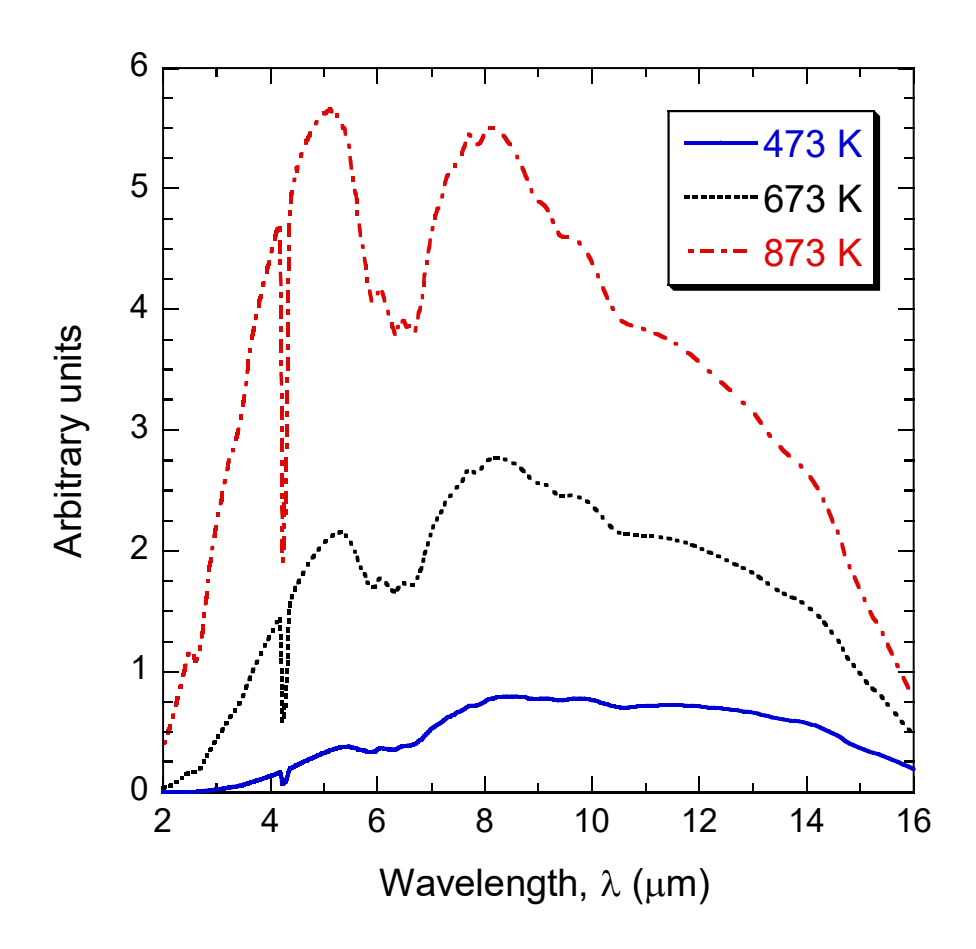
	СР		HSP	
	30/60	50/140	30/60	16/30
Ambient (300 K)	0.927	0.917	0.911	0.890
$T_{\rm cru} = 673 \text{ K}$	0.955 (587 K)	0.933 (582 K)	0.942 (591 K)	0.958 (586 K)
$T_{\rm cru} = 873 \text{ K}$	0.939 (716 K)	0.912 (711 K)	0.927 (726 K)	0.944 (719 K)

Figure captions

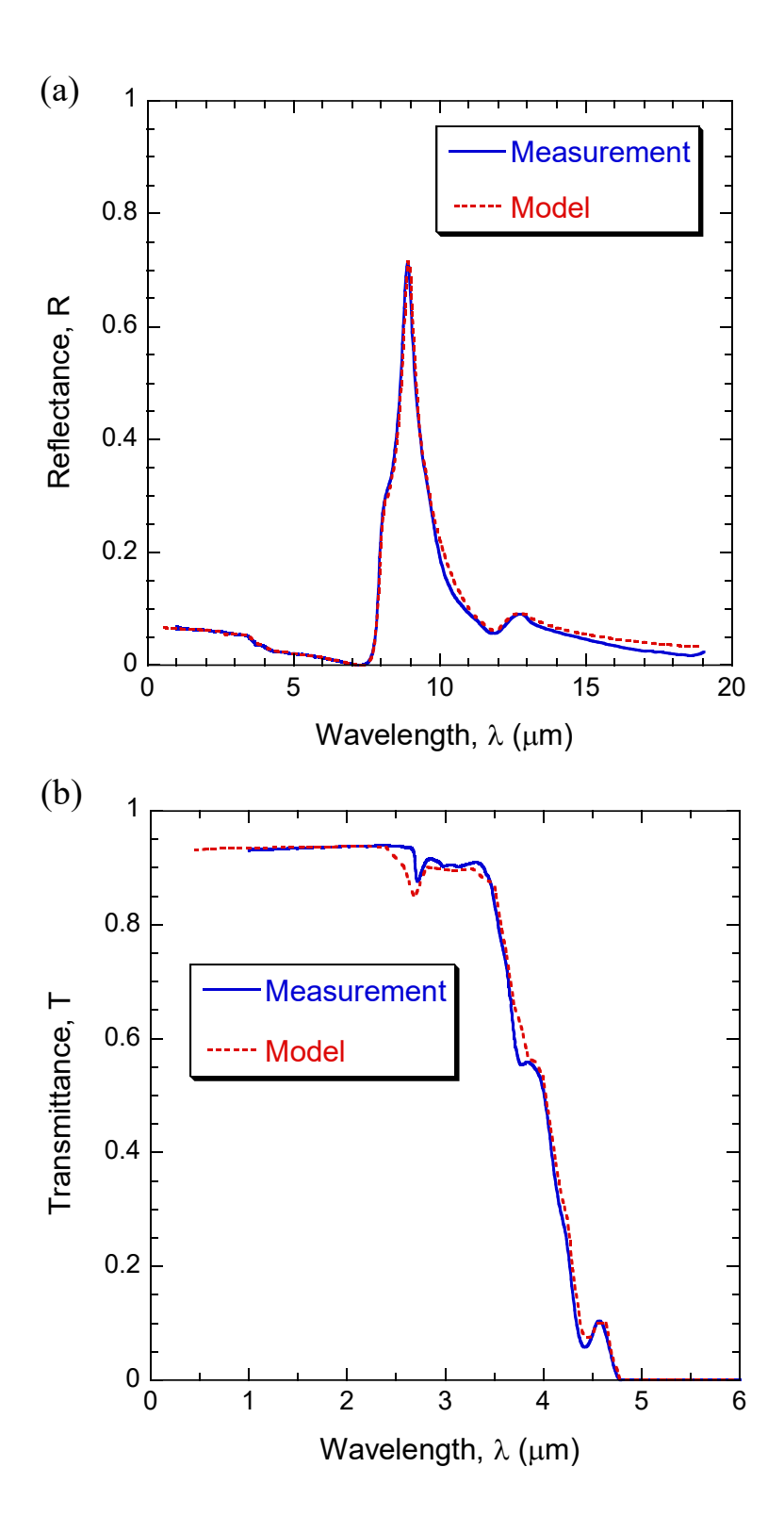
- Figure 1. Schematic of the high-temperature emissometer setup (not to scale). (a) Top view of the optical layout; (b) side view of the sample chamber.
- Figure 2. Measured blackbody signal spectrum at blackbody temperatures of 473, 673, and 873 K.
- Figure 3. Measured radiative properties of a 3-mm-thick fused silica disc at room temperature compared with modeling results. (a) reflectance; (b) transmittance.
- Figure 4. Temperature-dependent emittance of a 3-mm-thick fused silica disc compared with predictions using optical constants from Lorentz oscillator model for T = 300, 446, 610, and 769 K. (a) measurement; (b) modeling results
- Figure 5. Microscopic images of the particle beds used in the present study. (a) Four types of bauxite particles; (b) Wedron 410 polycrystalline silica particles.
- Figure 6. Measured temperature-dependent emittance of the silica particle bed ($d = 222 \mu m$) for T = 300, 435, 583,and 713 K.
- Figure 7. Measured temperature-dependent emittance of bauxite particle beds for Carbobead CP particles at various temperatures and sizes. (a) CP 30/60 ($d = 453 \mu m$) for T = 300, 587, and 716 K; (b) CP 50/140 ($d = 194 \mu m$) for T = 300, 582, and 711 K.
- Figure 8. Measured temperature-dependent emittance of bauxite particle beds for Carbobead HSP particles at various temperatures and sizes. (a) HSP 30/60 ($d = 495 \mu m$) for T = 300, 591, and 726 K; (b) HSP 16/30 ($d = 956 \mu m$) for T = 300, 586, and 719 K.



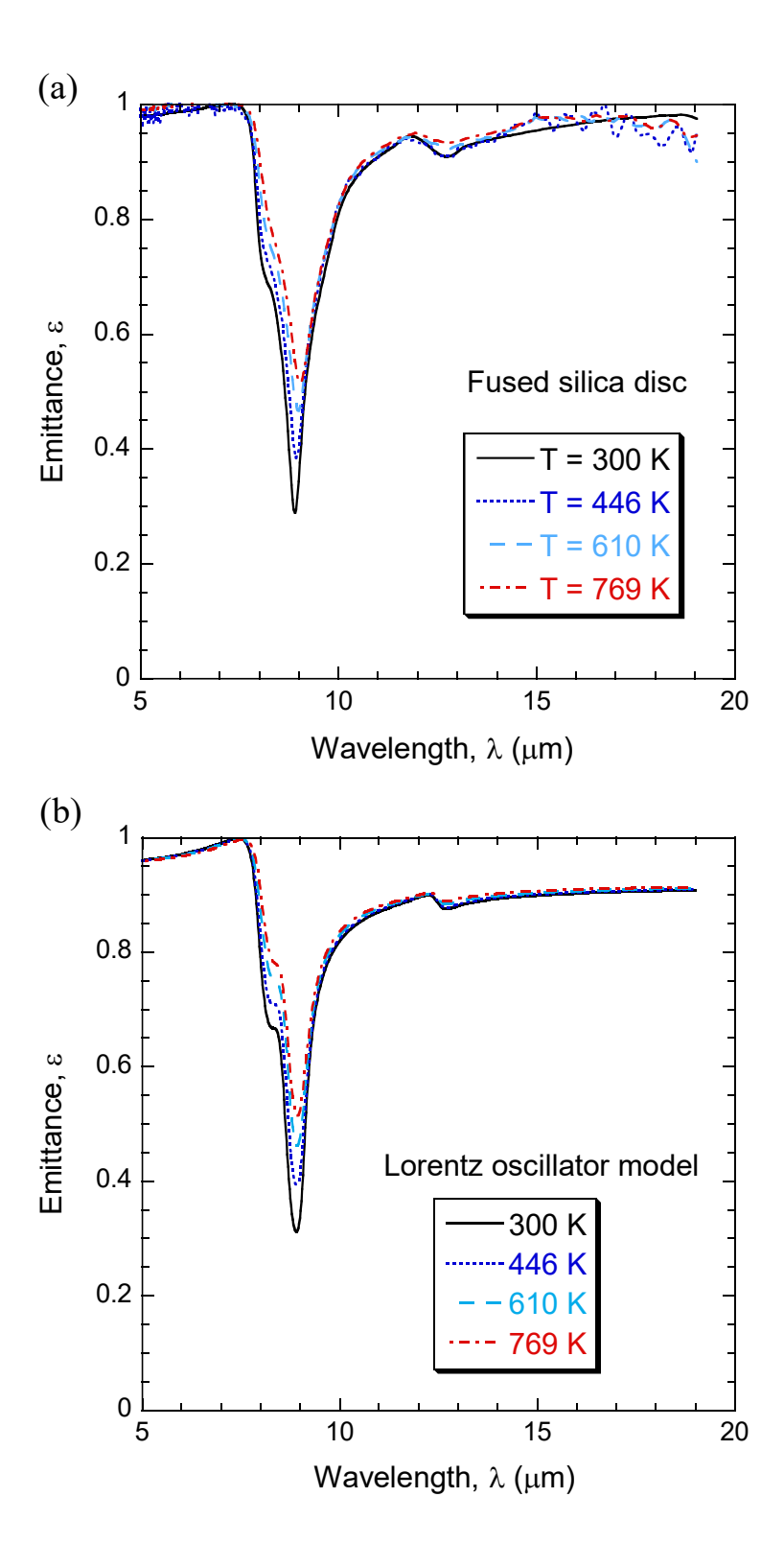
Chen et al. Figure 1



Chen et al. Figure 2



Chen et al. Figure 3

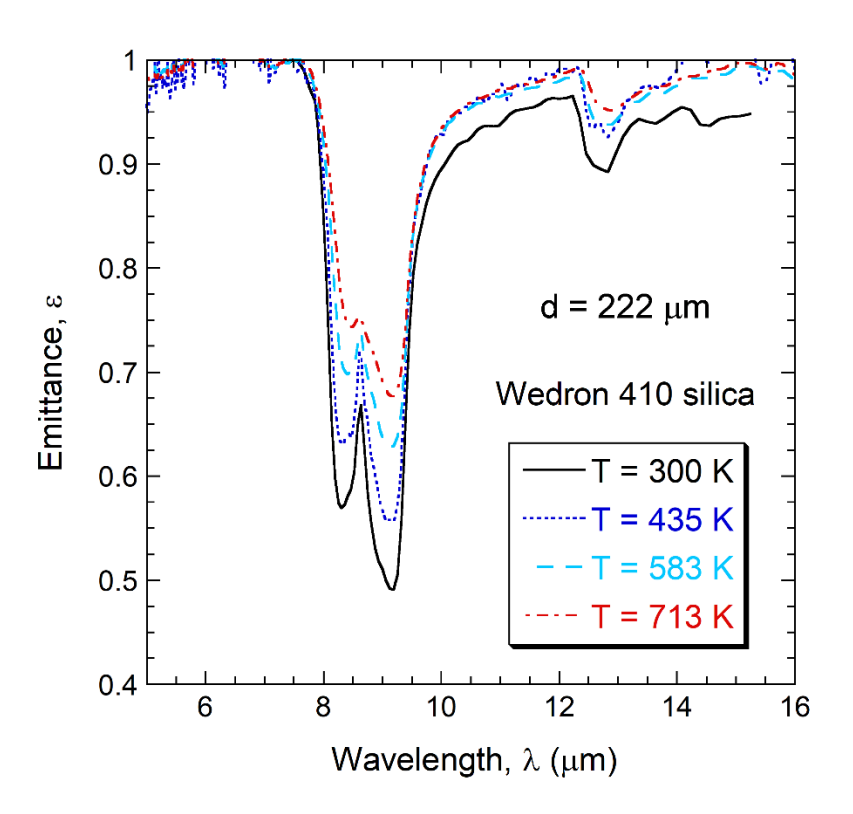


Chen et al. Figure 4

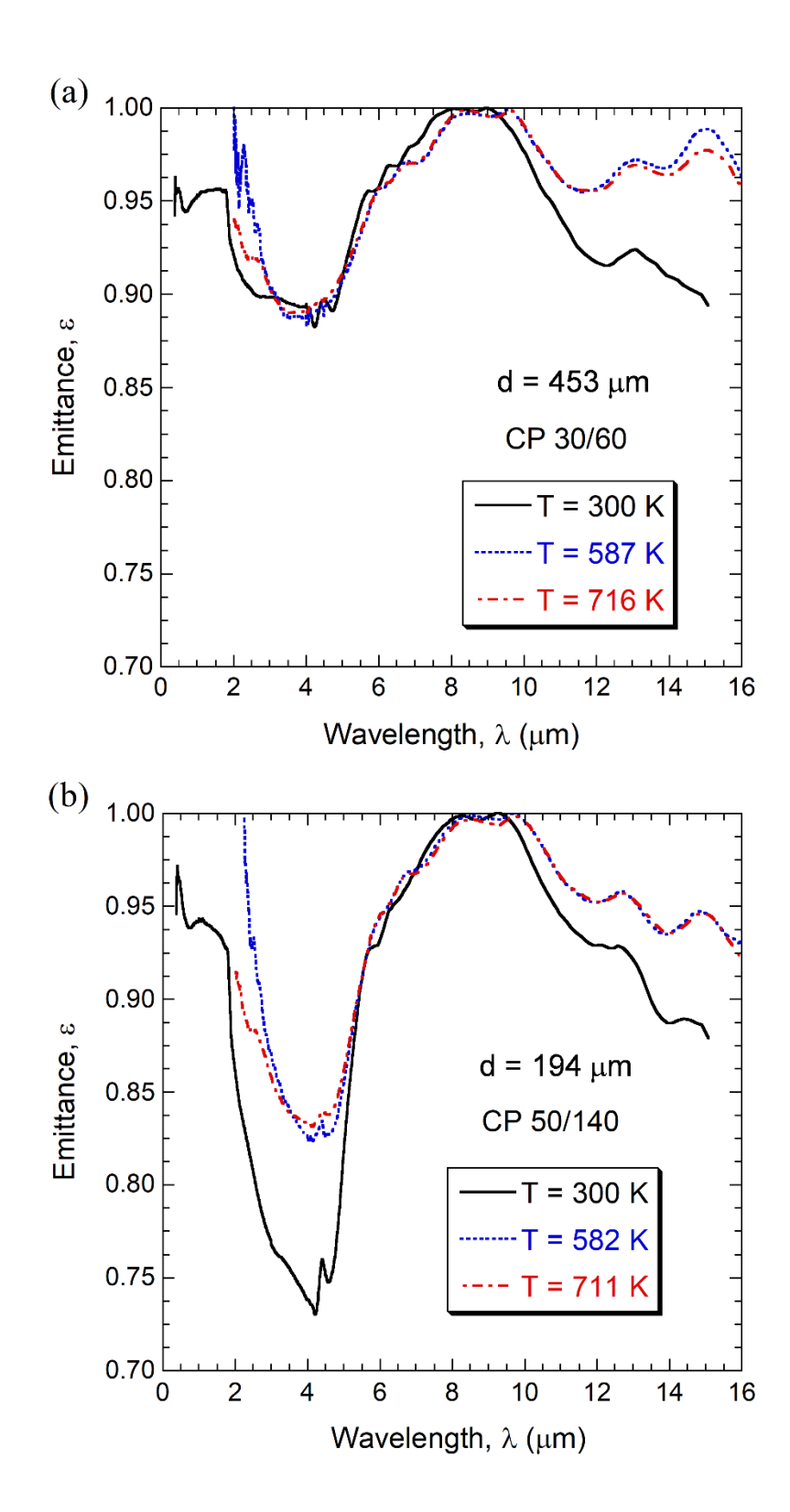




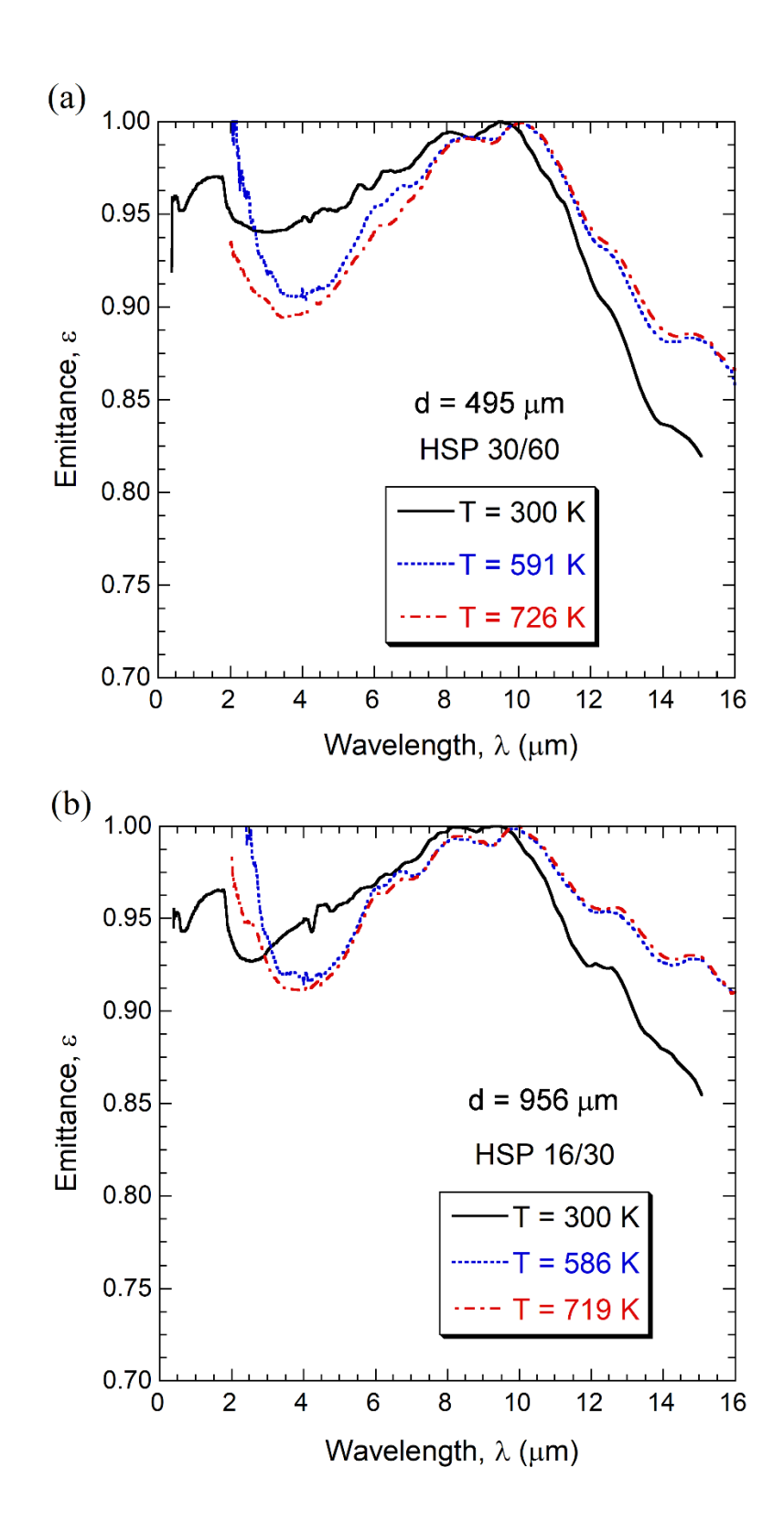
Chen et al. Figure 5



Chen et al. Figure 6



Chen et al. Figure 7



Chen et al. Figure 8